SCIENTIFIC REP**O**RTS

OPEN

Structural Properties and Sensing Performance of CeY$_x$O$_y$ Sensing Films for Electrolyte–Insulator–Semiconductor pH Sensors

Tung-Ming Pan[1,2], Chih-Wei Wang[1] & Ching-Yi Chen[1]

In this study we developed CeY$_x$O$_y$ sensing membranes displaying super-Nernstian pH-sensitivity for use in electrolyte–insulator–semiconductor (EIS) pH sensors. We examined the effect of thermal annealing on the structural properties and sensing characteristics of the CeY$_x$O$_y$ sensing membranes deposited through reactive co-sputtering onto Si substrates. X-ray diffraction, atomic force microscopy, and X-ray photoelectron spectroscopy revealed the structural, morphological, and chemical features, respectively, of the CeY$_x$O$_y$ films after their annealing at 600–900 °C. Among the tested systems, the CeY$_x$O$_y$ EIS device prepared with annealing at 800 °C exhibited the highest sensitivity (78.15 mV/pH), the lowest hysteresis voltage (1.4 mV), and the lowest drift rate (0.85 mV/h). Presumably, these annealing conditions optimized the stoichiometry of (CeY)O$_2$ in the film and its surface roughness while suppressing silicate formation at the CeY$_x$O$_y$–Si interface. We attribute the super-Nernstian pH-sensitivity to the incorporation of Y ions in the Ce framework, thereby decreasing the oxidation state Ce (Ce^{4+} → Ce^{3+}) and resulting in less than one electron transferred per proton in the redox reaction.

Due to increasing demands in environmental protection, health care and bio-nano technology, chemical- and bio-sensors based on semiconductors attract much attention as they can be miniaturized and integrated into small size electronic equipment for real time detection with high sensitivity. A dramatic change in the miniaturization of ion-selective membrane technology occurred when Bergveld demonstrated an ion-sensitive field-effect transistor (ISFET) by modifying a metal-oxide-semiconductor field-effect transistor (MOSFET) to expose the gate oxide film to an electrolyte solution[1, 2]. The theoretical chemical response of an ISFET sensor is the same as that of an ion-selective electrode. This sensor is replaced the fragile glass electrode with various gate oxides to detect a variety of ions. Since then, ISFETs offered several major advantages, including small size, rapid response, low output impedance, multiple ion sensor capability, and high compatibility for integration with complementary metal-oxide-semiconductor (CMOS) systems[3, 4]. Apart from ISFET, electrolyte-insulator-semiconductor (EIS) sensors without source and drain electrodes have relatively simpler structures and are easier to fabricate than ISFET devices. It is based on a MOSFET device without a metal gate for direct immersion in a buffer solution, the gate insulator material is a critical part of an ISFET or EIS device. The first sensitive pH response was attained with a SiO$_2$ membrane. Later, several metal oxide materials (e.g. Al$_2$O$_3$, Ta$_2$O$_5$, SnO$_2$, WO$_3$[5–9]) were used as sensing membranes because these materials possess large surface areas and good sensing performance. In addition to conventional metal oxides, a number of refractory oxides having high-dielectric constants (high-κ), such as TiO$_2$, ZrO$_2$, HfO$_2$, and Y$_2$O$_3$[10–12], have been received considerable attention as pH-sensitive membranes for promising applications in ISFET and EIS devices due to their good sensing properties. Nevertheless, their structures are generally unstable and very reactive for long-term and higher temperature applications as a result of the formation of a interfacial layer between the high-k metal oxide and the Si substrate in their manufacture. The interface layer can affect not only the performance an EIS sensor but also the sensor inoperable. Consequently, it is needed to find new materials and alternative processes to diminish interfacial defects.

Rare earth (RE) oxide films are possible replacements for traditional SiO$_2$ as the gate dielectric in advanced CMOS devices because of their large values of κ, lower leakage currents, high resistivities, and good thermal

[1]Department of Electronics Engineering, Chang Gung University, Taoyuan, 33302, Taiwan. [2]Division of Urology, Chang Gung Memorial Hospital, Taoyuan, 33302, Taiwan. Correspondence and requests for materials should be addressed to T.-M.P. (email: tmpan@mail.cgu.edu.tw)
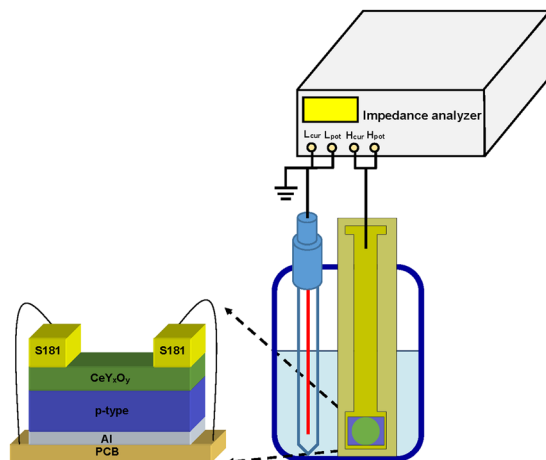
Figure 1. Schematic representation of the structure of a CeY$_x$O$_y$ EIS sensor.

stabilities[13–15]. We have previously reported the structural properties and sensing characteristics of several RE oxide films (e.g., Pr$_2$O$_3$, Nd$_2$O$_3$, Sm$_2$O$_3$, Er$_2$O$_3$) that behave as sensing membranes[16–19]. Among them, CeO$_2$ thin films have several advantages, including strong adhesion, high refractive index, good redox, high mechanical strength, excellent thermal stability, for applications in humidity sensors, fuel cells, and gas sensors[20–22]. Ansari *et al.*[23] also demonstrated that the nanostructured CeO$_2$ film was deposited on Au electrode using the sol-gel method for glucose sensor. Besides the above properties, they possess a high dielectric constant, a small lattice mismatch with silicon, and good thermodynamic stability in contact with silicon, making them particularly attractive materials for use as alternative gate dielectrics in nano-CMOS, flash memory, and EIS devices[24–26]. The major concern when using RE oxide films as sensing membranes, however, is prone to moisture absorption due to their hygroscopic nature, which degrades permittivity through the formation of low-permittivity hydroxides. The moisture absorption of RE oxide films stems from the presence of oxygen vacancies in the films[27]. To address this issue, several researchers in literatures[27, 28] have reported the incorporation of other elements (e.g., Ti, TiO$_x$, Y) into RE dielectric films which suppress the moisture absorption of the RE oxide. In this concern, we have reported Ti-doped RE oxide sensing membranes in our earlier works[29–31] which addresses the high hygroscopic nature of the RE oxide. The structural and sensing properties of CeY$_x$O$_y$ films as sensing membranes for EIS pH sensors have yet to be studied. In this work, we propose a CeY$_x$O$_y$ sensing film displaying super-Nernstian pH-sensitivity for use in EIS pH sensors. We have investigated the effects of thermal annealing on the structural properties and sensing characteristics of CeY$_x$O$_y$ thin films deposited on Si substrates through reactive co-sputtering. Moreover, we have employed X-ray diffraction (XRD), X-ray photoelectron spectroscopy (XPS), and atomic force microscopy (AFM) to monitor the quality of the CeY$_x$O$_y$ sensing films and determine the optimal annealing conditions. We measured the sensing characteristics (pH sensitivity, hysteresis, and drift) of these CeY$_x$O$_y$ films. The sensitivity of one such CeY$_x$O$_y$ EIS sensor (78.15 mV/pH) was higher than that expected from the Nernst law (59.2 mV/pH). We attribute this super-Nernstian response to the incorporation of Y ions into the Ce framework, thereby decreasing the oxidation state of Ce (Ce^{4+} → Ce^{3+}) and forming a mixed state of oxidized and reduced CeO$_x$ in the solution; as a result, less than one electron per proton would be transferred in the redox reaction.

Methods

Fabrication. EIS device structures incorporating CeY$_x$O$_y$ sensing films were fabricated on 4-in p-type (100) Si wafers. Prior to deposition of the CeY$_x$O$_y$ film, the wafer was cleaned through standard RCA cleaning and then treated with 1% HF to remove the native oxide. Subsequently, ~60 nm CeY$_x$O$_y$ film was deposited on the Si substrate through rf co-sputtering from cerium oxide and yttrium targets with a mixture of Ar and O$_2$ (Ar:O$_2$ = 25:5) ambient during sputtering. During the sputtering of CeY$_x$O$_y$ film, the rf power of CeO$_2$ and Y targets was 150 and 150 W, respectively. The chamber pressure was maintained at ~10^{-2} Torr and the deposition rate of the film was ~1.5 nm/min. The samples were subjected to rapid thermal annealing (RTA) in O$_2$ ambient for 30 s at 600, 700, 800, or 900 °C to achieve a crystalline (CeY)O$_2$ film. To form a backside contact, the backside SiO$_2$ layer was removed in a buffer oxide etchant (BOE) and then an Al film (400 nm) was deposited using a thermal evaporator. To define the sensing area of the deposited CeY$_x$O$_y$, an automatic robotic dispenser was used with an adhesive silicone gel (S181) acting as a segregating layer. The EIS device was assembled on a Cu wire on a custom-made printed circuit board by silver glue. To avoid leakage of the electrolyte, adhesive epoxy was encapsulated between EIS film and the Cu. The structure of the fabricated CeY$_x$O$_y$ EIS device is illustrated in Fig. 1.

Characterization. After RTA, the structural and compositional properties of the CeY$_x$O$_y$ sensing films were investigated using a combination of XRD and XPS. The XRD patterns were recorded on a Bruker D8 discover diffractometer with Cu K$_\alpha$ radiation (λ = 0.1541 nm) in a scanning angle (2θ) range of 20–60° at a scanning speed of 1° min^{-1}, operated at 40 kV and 40 mA, respectively. XPS was conducted using a Physical Electronics Quantum 2000 scanning ESCA microprobe, with a focused monochromatic Al K$_\alpha$ X-ray (1486.7 eV) source for excitation and a spherical section analyzer. Curve fitting of XPS spectra was performed using a Shirley background and
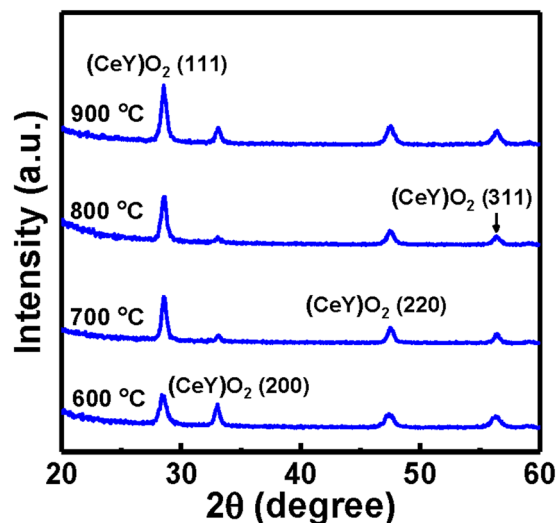
Figure 2. XRD patterns of CeY$_x$O$_y$ films that had been annealed at various temperatures.

a nonlinear least-squares curve-fitting program with a Gaussian/Lorentzian product function. The Gaussian/Lorentzian mixture was set at 0.5. The binding energies were calibrated by setting the value for the C 1 s orbital to 285 eV; they are accurate to within ± 0.2 eV. AFM images of the surfaces of the CeY$_x$O$_y$ films were recorded in air using a Solver P47 instrument (Russian NT-MDT), with a silicon probe operated in tapping mode. Surface roughnesses were determined from images obtained over an area of 3 × 3 μm^2.

Measurement. The pH-sensitivity of the CeY$_x$O$_y$ sensing films was determined by measuring the capacitance–voltage (C–V) curves of their EIS devices against pH buffer solutions (Merck), using a Ag/AgCl reference electrode and a Hewlett–Packard (HP) 4284 A LCR meter (ac signal frequency: 500 Hz); to avoid interference from light and noise, each experiment was performed in the dark at room temperature.

Results and Discussion

Structural Properties. In order to explore the microstructure of the annealed CeY$_x$O$_y$ sensing films, XRD measurements were carried out. It was found that the sharpness, intensity, and orientation of the diffraction peaks were sensitive to the thermal annealing condition. In Fig. 2, we show the XRD patterns of CeY$_x$O$_y$ sensing films for four different annealing temperatures, namely, 600 °C, 700 °C, 800 °C and 900 °C. Changes in the XRD patterns of the samples due to the thermal annealing can be seen clearly in Fig. 2. The diffraction peaks of all the films assigned to the (111), (200), (220), and (311) planes are indexed to the face-centered cubic structure of (CeY)O$_2$ crystals. The XRD pattern of the film annealed at 600 °C featured a strong (CeY)O$_2$ (111) peak, (CeY)O$_2$ (200) peak, and two weak (CeY)O$_2$ (220) and (311) peaks. RTA improved the crystalline structure of the (CeY)O$_2$ films. The intensity of the (CeY)O$_2$ (111) peak increased upon increasing the RTA temperature, consistent with a more crystalline CeY$_x$O$_y$ structure. A strong (CeY)O$_2$ (111) peak, (CeY)O$_2$ (200) peak, and two weak (CeY)O$_2$ (220) and (311) peaks appeared in the patterns of the samples that had been annealed at 800 and 900 °C, suggesting the formation of a stoichiometric (CeY)O$_2$ film. We attribute this annealing behavior to the Y atoms reacting with CeO$_x$ to provide a more stoichiometric CeY$_x$O$_y$ structure.

The morphology of the CeY$_x$O$_y$ films prepared at various temperatures is revealed by AFM images. Figure 3 displays AFM surface images of CeY$_x$O$_y$ films that had been annealed at different temperatures. The surface roughness (rms) values of 1.77, 1.81, 1.92, and 252 nm were determined for the CeY$_x$O$_y$ films treated at 600, 700, 800, and 900 °C, respectively. It can be see that the surface roughness value increased with increasing the annealing temperature. This behavior is attributed to the aggregation of the native grains into the larger clusters upon annealing[32]. This different cluster size affects the surface morphology of the films. The surface roughnesses of the CeY$_x$O$_y$ films annealed at the various RTA temperatures were consistent with the intensities of the diffraction peaks in Fig. 2; therefore, the AFM and XRD data are in good agreement. Figure 3(d) depicts that the CeY$_x$O$_y$ film annealed at 900 °C had larger clusters and becomes rougher. We suspect that self-diffusion of Ce and Y atoms increased during high-temperature annealing, enhancing the clustering of grains and, thereby, increasing the surface roughness of the CeY$_x$O$_y$ film. An increase in grain size might improve the sensing performance when the film was used for the membrane. In contrast, Fig. 3(a) demonstrates that the CeY$_x$O$_y$ film at 600 °C featured smaller grains and showed smoother surface.

To further investigate the surface composition and chemical states, the CeY$_x$O$_y$ films after RTA at various temperatures were performed by XPS technique. The Ce 3d, Y 3d, and O 1 s spectra of the CeY$_x$O$_y$ films prepared at different temperatures are shown in Fig. 4(a), (b) and (c), respectively. The Ce 3d$_{5/2}$ spectra in Fig. 4(a) can be deconvoluted into three peaks: v (~882.6 eV), v' (~884.7 eV) and v'' (~888.9 eV). The 3d^{10}4f^0 state of Ce^{4+} species are labeled as v and v'', whereas the 3d^{10}4f^1 state of Ce^{3+} is represented as v'[33]. The binding energy of the Ce 3d$_{5/2}$ peak at 882.1 eV[34] for the CeO$_2$ film is taken as energy reference, while that at 885.3 eV is assigned to the Ce$_2$O$_3$ structure[34]. Three v, v' and v'' peak binding energies exhibit quite similar evolutions, indicating no samples
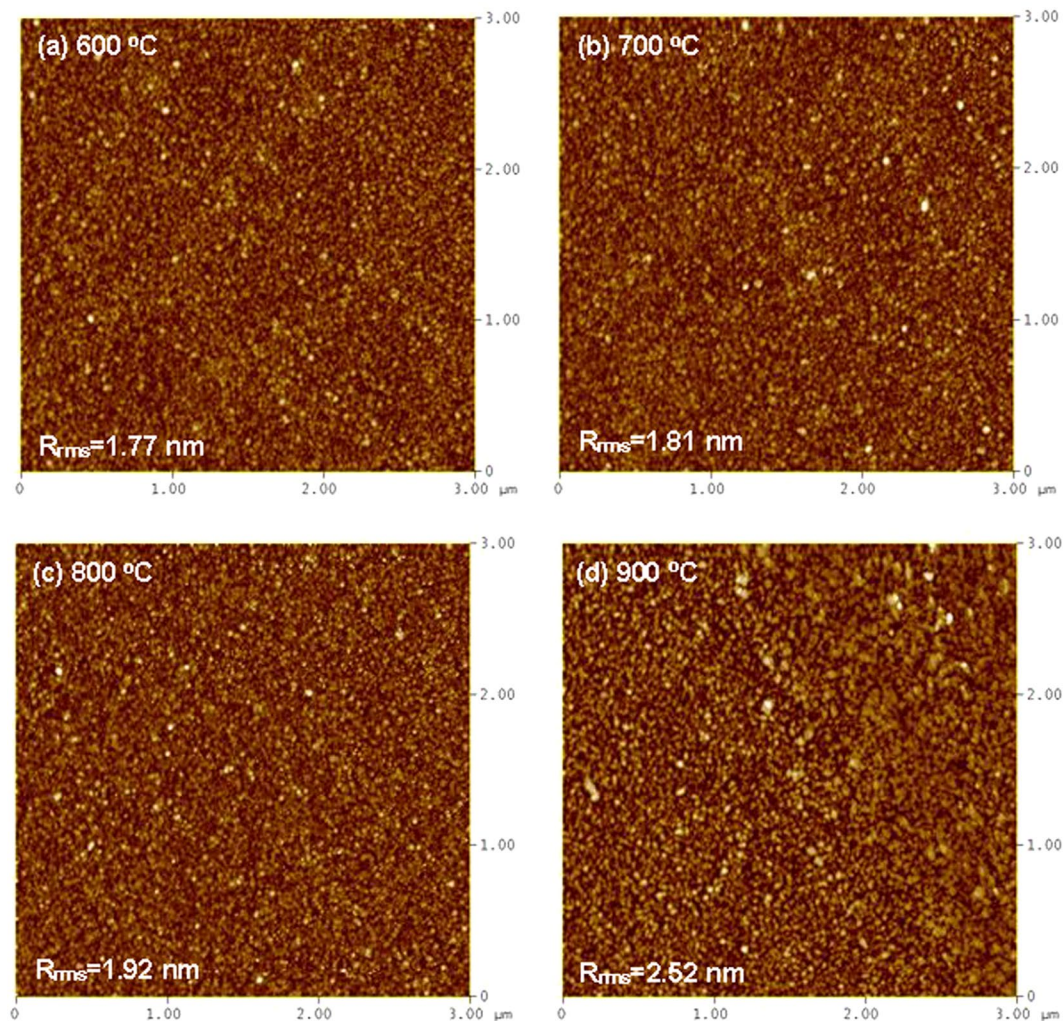
Figure 3. AFM surface images of CeY$_x$O$_y$ sensing films that had been annealed at (**a**) 600, (**b**) 700, (**c**) 800, and (**d**) 900 °C.

modification with depth. From Fig. 4, it is found that the main chemical valence of cerium for + 4 oxidation state and a small amount of + 3 oxidation state co-existed in the film. The effective ionic radii of Ce^{4+}, Ce^{3+} and Y^{3+} are 0.97, 1.14 and 1.01 Å[35], respectively. The + 3 oxidation state of cerium was introduced by the spontaneous trans-formation of smaller radius Ce^{4+} due to larger radius Ce^{3+}, the addition of smaller radius Y^{3+} can compensate the lattice expansion induced by larger Ce^{3+} ions. A shift of the v peak position toward lower binding energy, from 882.6 to 882.3 eV, prepared upon increasing the RTA from 600 to 900 °C, indicative of reactions of the Ce and Y atoms with O atoms to form a stoichiometric (CeY)O$_2$ structure. For the film annealed at 600, 700 and 800 °C, the v' and v'' peak positions of were fixed at 884.7 and 888.9 eV, but 900 °C-annealed sample suddenly shifted toward lower binding energy by 0.3 and 0.2 eV, respectively. It was thus interpreted that the deposited CeY$_x$O$_y$ film undergoes solid-phase intermixing with Si from the substrate during high-temperature annealing to form a Ce-silicate layer. The silicate layer is speculated to result from reactions between silicon and CeO$_x$ formed at the surface of oxide film and Si substrate. The Y 3d$_{3/2}$ and 3d$_{5/2}$ double peaks of the Y$_2$O$_3$ reference appeared at 158.5 and 156.7 eV[36], respectively. Figure 4(b) displays these signals for the film annealed at 600 °C, at 158.9 and 157 eV, respectively, suggesting a poor (CeY)O$_2$ structure incorporating Y in the form of CeY(OH)$_x$, which probably formed at the surface of the sample during its exposure to air. The positions of the Y 3d$_{3/2}$ and 3d$_{5/2}$ peaks shifted to higher binding energies upon increasing the annealing temperature. For the sample subjected to RTA at 800 °C, the binding energies of the Y 3d$_{3/2}$ and 3d$_{5/2}$ orbitals were 159.1 and 157.2 eV, respectively, reflecting the presence of (CeY)O$_2$ structures. The intensities of the Y 3d$_{3/2}$ and 3d$_{5/2}$ split peaks provided by CeY$_x$O$_y$ remained quite constant for annealing temperatures of up to 800 °C, but the former increased suddenly while the latter decreased after annealing at 900 °C. This phenomenon is consistent with the reactions of Ce atoms with O and Si atoms to form a thicker Ce-silicate layer. Figure 4 (c) presents the O 1 s spectra for the annealed CeY$_x$O$_y$ films, with appro-priate curve-fitting of the peaks. The O 1 s peak of the Ce$_2$O$_3$ reference appeared at 530.6 eV[37]. In the three spectra, the O 1 s peaks at 533.4, 531.5 (531.4 eV for 700 and 800 °C, 531.6 eV for 900 °C), and 530.6 eV (530.7 eV for 800 and 900 °C) represent the Ce–OH, Ce–O–Y, and Ce–O bonds, respectively. For 600 °C-annealed sample, the O
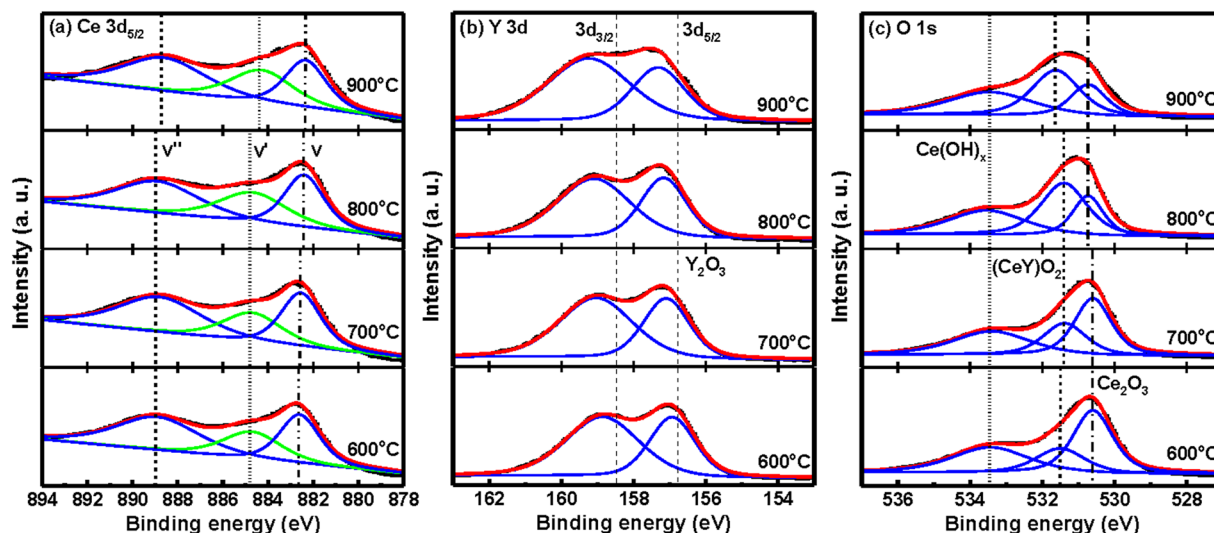
Figure 4. XPS spectra displaying the (**a**) Ce 3d, (**b**) Y 3d, and (**c**) O 1 s energy levels in CeY$_x$O$_y$ films that had been annealed at various temperatures.

1 s peak intensities provided by Ce(OH)$_x$ was larger compared to other annealing temperatures, respectively. This result may be attributed a poor CeY$_x$O$_y$ film to the hydroxide formation after exposure to an air ambient. The moisture absorption of RE oxide film may be attributed to the metal defects or oxygen vacancies in the films[38]. The intensity of the O 1 s peak corresponding to (CeY)O$_2$ increased upon increasing the RTA temperature— except at 900 °C, where it decreased relative to the signal for Ce$_2$O$_3$. This behavior suggests that Ce and Y atoms reacted with O atoms to form a stoichiometric (CeY)O$_2$ film. For the CeY$_x$O$_y$ component of the sample annealed at 900 °C, the O 1 s peak shifted to higher binding energy by 0.1 or 0.2 eV relative to those of the samples subjected to the other annealing temperatures. In addition, the intensity of the O 1 s peak for the Ce$_2$O$_3$ component of the sample annealed at 900 °C was weaker than other RTA temperatures. During high-temperature annealing, the Ce atoms diffused readily from the CeO$_x$ film to form a thicker Ce-silicate layer at the CeY$_x$O$_y$–Si interface[39].

Sensing Characteristics.   The metal gate of the MOSFET is replaced by a reference electrode, while the liquid in which this electrode is present makes contact with the gate oxide. In case of an ISFET the gate voltage is the voltage at the reference electrode, usually grounded reference electrode, but the threshold voltage comprises also terms which reflect the interfaces between the liquid and the gate oxide on the one side and the liquid and the reference electrode at the other side. The threshold voltage (V_{th}) of an ISFET device is defined by the equation[40]

$$V_{th} = E_{ref} - \psi + \chi^{sol} - \frac{\Phi_{Si}}{q} - \left(\frac{Q_{SS} + Q_{SC}}{C_{OX}} - 2\phi_{fp}\right).$$

(1)

where E_{ref} is the reference electrode potential relative to vacuum, ψ is the surface potential, which results from a chemical reaction, usually governed by the dissociation of oxide surface groups, χ^{sol} is the surface dipole potential of the solution, Φ_{Si} is the Si work function, q is the elementary charge, Q_{ss} is the surface state density at the Si sur- face, Q_{SC} is the depletion charge in Si, C_{ox} is the gate oxide capacitance per unit area, and ϕ_{fp} is the Fermi potential of semiconductor (p-type for the n-channel MOSFET considered here). All terms usually refer to constant but does not include ψ, because this term makes the ISFET sensitive to the electrolyte pH, which is controlling the dissociation of the oxide surface groups. Designing a pH sensitive ISFET with a maximum sensitivity needs there- fore a detailed study of the oxide-electrolyte interface to choose the best oxide film, which is not a priority for SiO$_2$ in MOSFETs. In an ISFET device, the change in the surface potential at the oxide–aqueous electrolyte interface will shift the threshold voltage. It is mainly related to the charge concentration, which can be interpreted using the site-binding model to characterize the properties of an oxide–electrolyte interface[41]. The surface of metal oxide usually contains hydroxyl groups. These groups can donate or accept a proton from the solution, leaving a neg- atively charged or a positively charged surface group, respectively. The equilibrium reactions can occur between protons in the solution and the hydroxyl groups formed at the oxide-solution interface. The mechanism respon- sible for the oxide surface charge can be explained by the site-binding model, which describes the equilibrium between the so-called amphoteric Si-OH surface sites and the H$^+$-ions in the solution. In the site-binding model, the terminal OH groups on the surface of the gate oxide can be neutral in the form (OH), protonated (OH$_2^+$; i.e., accepted a proton), or deprotonated (O$^-$; i.e., donated a proton) at the oxide–electrolyte interface. At low pH (high proton concentration in solution), the equilibrium is shifted toward a protonated (i.e., positively charged) surface, which becomes a positive site. As a result, the C–V curve is shifted to the right direction. Around the point of zero charge, a general expression for the pH sensitivity of an ISFET sensor is given by[41]
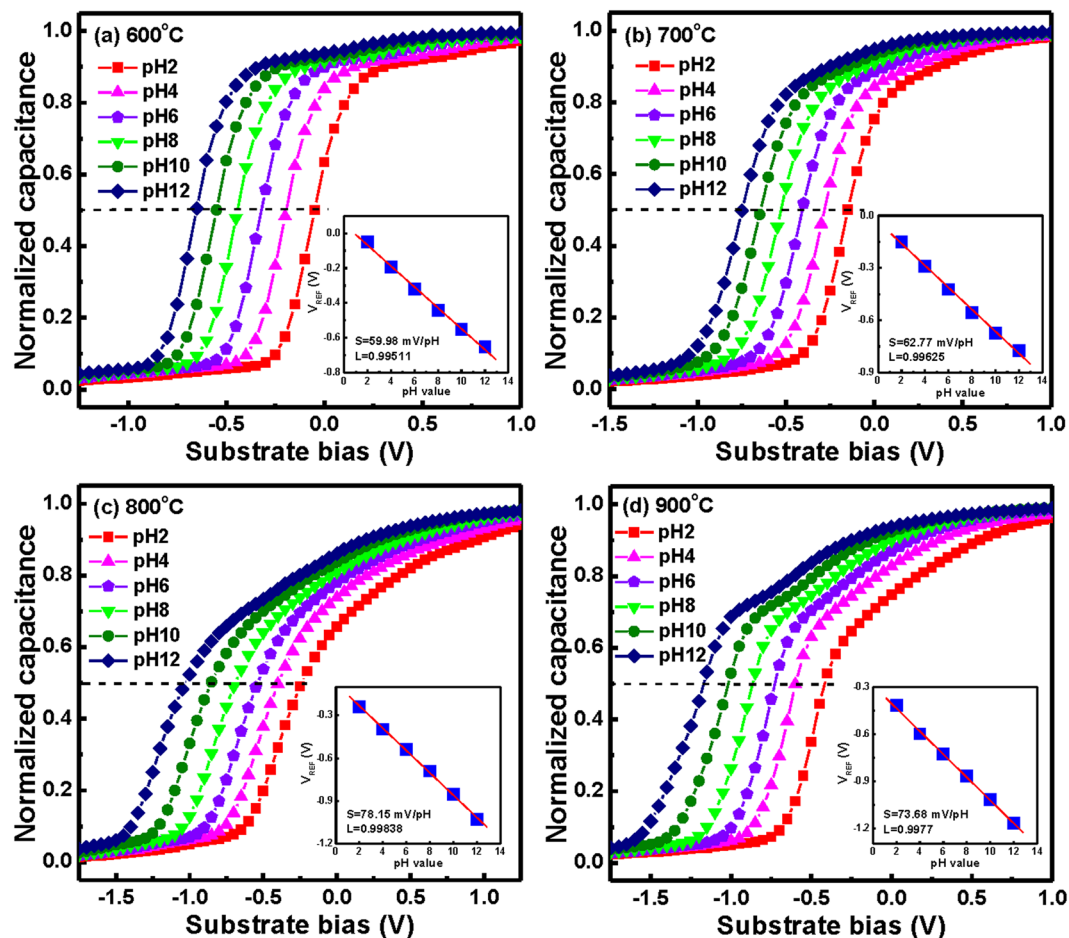
Figure 5. Responses of the $C-V$ curves for CeY_xO_y EIS sensors that had been prepared with annealing at (**a**) 600, (**b**) 700, (**c**) 800, and (**d**) 900 °C. Insets: Reference voltages plotted with respect to pH for the CeY_xO_y EIS sensors.

$$\frac{d\psi}{dpH} = 2.303\frac{kT}{q}\frac{\beta}{\beta + 1} \tag{2}$$

where k is Boltzmann's constant, T is the absolute temperature, and β is a parameter that denotes the chemical sensitivity of the gate oxide and is proportional to the density of reactive sites, given by

$$\beta = \frac{2q^2N_s\sqrt{K_aK_b}}{kTC_{DL}} \tag{3}$$

where N_s is the total number of surface sites per unit area, K_a and K_b are the equilibrium constants at the acid and base point, respectively, and C_{DL} is the double-layer capacitance derived from the Gouy–Chapman–Stern model[42]. In this model, the double-layer capacitance consists of a series network of a Helmholtz-layer capacitance (the Stern capacitance) and a diffuse-layer capacitance. The Helmholtz layer model indicate that the ions in the solution have a finite size and the centers of the ions cannot approach the surface any closer compared with the ionic radius (including a possible water layer). The diffuse layer comprises the same amount of charge (of opposite sign) as the oxide surface charge, since the Helmholtz layer is by definition no containing any charge. If β parameter approaches infinite, the ISFET has a theoretical maximum value of accurately 59.6 mV/pH at 300 K, which is also called the maximum Nernstian sensitivity.

To achieve the high sensitivity of an EIS sensor, we evaluated the sensing performance of the CeY_xO_y EIS devices annealed at various temperatures. Figure 5(a–d) display the pH-dependence of a group of $C-V$ curves for the CeY_xO_y EIS devices prepared with annealing at 600, 700, 800, and 900 °C, respectively, and measured at values of pH in the range from 2 to 12. The change in the number of hydrogen ions on the sensing films led to shifts in the normalized $C-V$ curves. We attribute the kinks in the $C-V$ curves to the presence of interface traps between the CeY_xO_y film and Si substrate[43]. Here, the reference voltage (V_{REF}) for each pH buffer solution was the voltage required to obtain a normalized capacitance of 0.5. The insets to Fig. 5 (a–d) display the V_{REF} as function of pH values for the CeY_xO_y EIS devices that had been prepared with the various annealing temperatures. The

pH-sensitivities of the CeY_xO_y films after RTA at 600, 700, 800, and 900 °C were determined to be 59.98, 62.77, 78.15, and 73.68 mV/pH, respectively. Thus, among these tested systems, the CeY_xO_y EIS device annealed at 800 °C exhibited the highest sensitivity, possibly because of the higher surface roughness (AFM) of its CeY_xO_y sensing film. A higher surface roughness will increase the surface site density and, therefore, improve the detection sensitivity, as previously discussed for the site-binding model. Nevertheless, the sensitivity of the CeY_xO_y film annealed at 900 °C was lower than that of the film annealed at 800 °C, presumably because of a thicker silicate layer formed at the CeY_xO_y–substrate interface after treatment at such a high temperature[39]. Moreover, the pH-responses for the CeY_xO_y EIS sensors were higher than that expected (59.6 mV/pH) from the Nernst law, possibly because the addition of Y ions into the Ce framework enhanced the decrease in the Ce oxidation state ($Ce^{4+} \rightarrow Ce^{3+}$). The wide application of ceria (CeO_2) is driven by its ability to store and release oxygen (by creating oxygen vacancy sites) due to the easily accessible redox cycle of cerium ions ($Ce^{3+} \rightleftarrows Ce^{4+}$)[44].

During the oxygen release process, the volume of the Ce compound increases in proportion to the change in the Ce oxidation state from Ce^{4+} to Ce^{3+}. The stress energy resulting from this volume increase would enhance any further valence change of the Ce oxidation state. The introduction of Y ions into the Ce framework would compensate for the increase in volume and ease the change in valence of the Ce oxidation state. The potential response with respect to pH is related to the equilibrium between the oxidized and reduced forms of CeO_x. The hydroxyl groups can be considered as amphoteric sites, according to the site-binding theory, which can get or release a proton, for example:

$$CeO(OH) \leftrightarrows CeOO^- + H^+ \tag{4}$$

$$CeO(OH) + H^+ \leftrightarrows CeO(OH_2)^+ \tag{5}$$

$$2Ce(OH)_3 + H_2O \leftrightarrows Ce_2O(OH)_6 + 2H^+ + 2e^- \tag{6}$$

In Eqs (4–6), these reactions do not need electron transfer because the number of electrons transferred is equivalent to that of the protons (H^+). As a result, the pH-sensitivity is estimated to be 59 mV/pH when considering the redox potential[45]. Nevertheless, pH sensitivities of over 59 mV/pH have been measured for other electrodes (e.g., IrO_x, Ta_2O_5)[46, 47]. We suspect that a change in the Ce ion valence occurs during the reversible reaction from Ce^{4+} to Ce^{3+}. The film can be considered only as an acidic oxyhydroxide, which the amphoteric character of the hydroxyl groups can be neglected, each state of the film with its own degree of proton dissociation:

$$Ce(OH)_3 \leftrightarrows Ce(OH)_2O^- + H^+ \tag{7}$$

$$Ce_2O(OH)_6 \leftrightarrows Ce_2O(OH)_3O_3{}^{3-} + 3H^+ \tag{8}$$
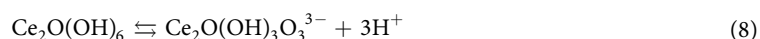
Substitution of redox reactions (7) and (8) into reaction (9) yields

$$2Ce(OH)_2O^- + H_2O \leftrightarrows Ce_2O(OH)_3O_3{}^{3-} + 3H^+ + 2e^- \tag{9}$$
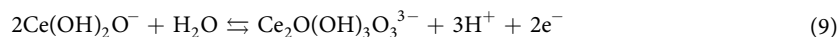
For this reaction, only two electrons are transferred for every three protons; in this case, the maximum slope for a Nernst equation could reach as high as 88 mV/pH[48]. Thus, experimental observations of pH sensitivities of greater than 59 mV/pH might be explained by considering mixed oxidized and reduced CeO_x states that lead to less than one electron per proton being transferred in the redox reaction. In contrast, for pH-sensitivities of less than 59 mV/pH, more than one electron would be transferred per proton. In this study, our CeY_xO_y films exhibited sensitivities to pH that are superior to those of sensing materials commonly used for ISFET and EIS sensors such as, Nb_2O_5 (52.12 mV/pH)[49], Y_2O_3 (54.5 mV/pH)[12], CeO_2 (58.76 mV/pH)[26], ZnO_2 (58 mV/pH)[50], Pr_2O_3 (52.9 mV/pH)[16], Nd_2O_3 (56.01 mV/pH)[17], Sm_2O_3 (56.2 mV/pH)[18], Er_2O_3 (57.58 mV/pH)[19], and $Eu_2Ti_2O_7$ (59.03 mV/pH)[29].

The hysteresis and drift phenomena of a gate insulator influence the performance of ISFET and EIS sensors. A surface-site model can describe hysteresis characteristics when assuming that a fraction of the sites will respond slowly to changes in pH[5] as a result of imperfections in the insulator film; these imperfections lead to porosity that produces interior sites that react with the ions in the solution. We tested our CeY_xO_y EIS capacitors through a pH loop of 7→4→7→10→7 over a period of 25 min. We define the hysteresis voltage as the difference in reference voltage between the initial (first pH 7) and terminal (last pH 7) voltages in the pH loop. Figure 6 presents the hysteresis voltages of CeY_xO_y EIS devices that had been prepared with annealing at various temperatures; they were immersed in buffer solutions having various values of pH in an alternating cycle (pH 7, pH 4, pH 7, pH 10, pH 7), for 5 min in each solution. The hysteresis voltage of the CeY_xO_y EIS devices annealed at 600, 700, 800, and 900 °C were 126.3, 5.9, 1.4, and 40.9 mV, respectively. Thus, the EIS sensor annealed at 800 °C exhibited the smallest hysteresis voltage (1.4 mV), while that annealed at 600 °C had the highest (126.3 mV). Defects and vacancies in the films may have caused ions to attach to the surface and, thereby, delay the response to the reference voltage. Annealing at 800 °C could diminish the extent of crystal defects and, thereby, minimize the number of attached ions on the surface during the test.

According to the physical model for gate voltage drift proposed by Jamasb et al.[51], the overall capacitance of gate insulator (the series combination of the capacitance of the modified surface layer and the underlying insulator) should exhibit a slow, temporal variation. Therefore, the amount of inversion charge stored in the semiconductor at a given gate bias would slowly change over time, leading to a monotonic temporal change in the threshold voltage and, thus, in the drain current; this phenomenon is commonly known as "drift." Chemical
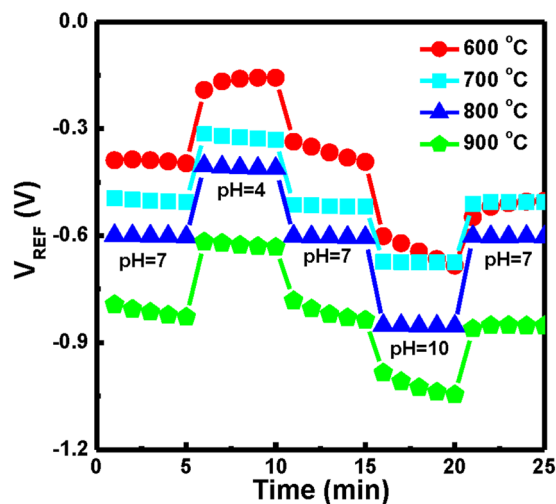
Figure 6. Hysteresis voltages during the pH loop 7→4→7→10→7 of CeY$_x$O$_y$ EIS devices that had been prepared with annealing at various temperatures.
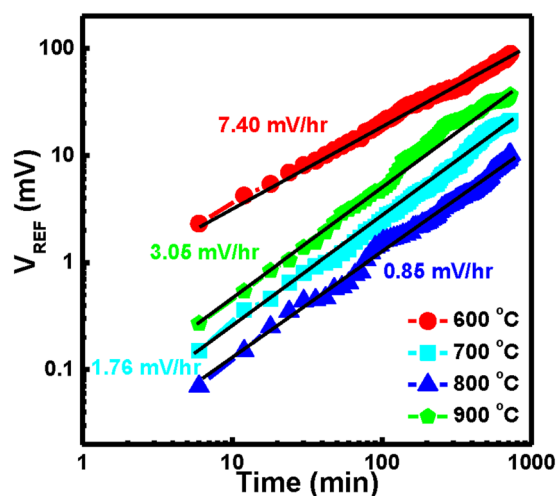

Figure 7. Drift rates measured in solution at pH 7 of CeY$_x$O$_y$ EIS sensors that had been prepared with annealing at various temperatures.

modification of the insulator surface can lead to a variation in the number of surface sites over time, thereby resulting in a monotonic temporal increase in the threshold voltage. Figure 7 displays the drift characteristics of the CeY$_x$O$_y$ EIS devices prepared with annealing at the various RTA temperatures, measured in solution at pH 7 for 12 h. Here, the change in the reference voltage (ΔV_{REF}) is defined as

$$\Delta V_{REF} = V_{REF}(t) - V_{REF}(0) \qquad (10)$$

The degradation slope of the reference voltage represents the EIS stability. The drift rates of the CeY$_x$O$_y$ EIS devices after RTA at 600, 700, 800, and 900 °C were 7.40, 1.76, 0.85, and 3.05 mV/h, respectively. Thus, the CeY$_x$O$_y$ EIS device annealed at 800 °C had the best long-term stability, while the device annealed at 600 °C exhibited a serious drift rate. The drift in the reference voltage might result from lattice defects (e.g., vacancies or dangling bonds) capturing clusters of ions. We suspect that the less-pronounced drift behavior after RTA at 800 °C arose from a lower density of crystal defects; that is, these annealing conditions could effectively remove such defects. In addition, a higher drift rate may be due to a larger number of crystal defects producing buried surface sites and/or traps.

Conclusion

We have observed a super-Nernstian response to pH from EIS devices incorporating CeY$_x$O$_y$ sensing membranes grown on Si substrates through reactive co-sputtering. XRD, XPS, and AFM confirmed the presence of (CeY)O$_2$ structures in these EIS devices. The pH-sensing performance of the EIS device incorporating the CeY$_x$O$_y$ film that had been annealed at 800 °C was superior to those of the devices subjected to other annealing

temperatures, including a higher sensitivity (78.15 mV/pH), a smaller hysteresis voltage (1.4 mV), and a lower drift rate (0.85 mV/h). This enhanced performance resulted from the formation of a stoichiometric $(CeY)O_2$ film, a high surface roughness, and a low number of crystal defects after applying these annealing conditions. The super-Nernstian pH-response appears to have resulted from the Y ions incorporated within the Ce framework enhancing the valence change of the Ce oxidation state, thereby causing less than one electron to be transferred per proton in the redox reaction, due to the mixed oxidized and reduced CeO_x states in the solution.

References

1. Bergveld., P. Development of an ion-sensitive solid-state device for neurophysiological measurements. *IEEE Trans. Biomed. Eng.* **17**, 70–71 (1970).
2. Bergveld, P. Development, operation, and application of the ion-sensitive field-effect transistor as a tool for electrophysiology. *IEEE Trans. Biomed. Eng.* **19**, 342–351 (1972).
3. Poghossian, A. & Poghossian, M. J. Detecting both physical and (bio-) chemical parameters by means of ISFET devices. *Electroanalysis* **16**, 1863–1872 (2004).
4. Bergveld, P. Thirty years of ISFETOLOGY: What happened in the past 30 years and what may happen in the next 30 years. *Sens. Actuators B* **88**, 1–20 (2003).
5. Bousse, L., Mostarshed, S., van der Schoot, B. & de Rooij, N. F. Comparison of the hysteresis of Ta_2O_5 and Si_3N_4 pH-sensing insulators. *Sens. Actuators B* **17**, 157–164 (1994).
6. Bousse, L., van der Vlekkert, H. H. & de Rooij, N. F. Hysteresis in Al_2O_3-gate ISFETs. *Sen. Actuators B* **2**, 103–110 (1990).
7. Chi, L. L., Chou, J. C., Chung, W. Y., Sun, T. P. & Hsiung, S. K. Study on extended gate field effect transistor with tin oxide sensing membrane. *Mater. Chem. Phys.* **63**, 19–23 (2000).
8. Ahmed, J. *et al.* Tin dioxide nanoparticles: Reverse micellar synthesis and gas sensing properties. *Mater. Res. Bull.* **43**, 264–271 (2008).
9. Chiang, J. L., Jan, S. S., Chou, J. C. & Chen, Y. C. Study on the temperature effect, hysteresis and drift of pH-ISFET devices based on amorphous tungsten oxide. *Sen. Actuators B* **76**, 624–628 (2001).
10. Chou, J. C. & Liao, L. P. Study of TiO_2 thin films for ion sensitive field effect transistor application with rf sputtering deposition. *Jpn. J. Appl. Phys. Part* **1**(43), 61–65 (2004).
11. Jankovic, V. & Chang, J. P. HfO_2 and ZrO_2–based microchemical ion sensitive field effect transistor (ISFET) sensors: Simulation & experiment. *J. Electrochem. Soc.* **158**, P115–P117 (2011).
12. Pan, T. M. & Liao, K. M. Influence of oxygen content on the structural and sensing characteristics of Y_2O_3 sensing membrane for pH-ISFET. *Sen. Actuators B* **128**, 245–251 (2007).
13. Engstrom, O. *et al.* Navigation aids in the search for future high-k dielectrics: Physical and electrical trends. *Solid State Electron.* **51**, 622–626 (2007).
14. Paivasaari, J., Putkonen, M. & Niinisto, L. A comparative study on lanthanide oxide thin films grown by atomic layer deposition. *Thin Solid Films* **472**, 275–281 (2005).
15. Scarel, G., Svane, A. & Fanciulli, M. *Rare Earth Oxide Thin Films: Growth, Characterization, and Applications* (ed. Fanciulli, M. & Scarel, G.) Ch. 1, 1-14 (Springer, 2007).
16. Pan, T. M. & Liao, K. M. Comparison of structural and sensing characteristics of Pr_2O_3 and $PrTiO_3$ sensing membrane for pH-ISFET application. *Sen. Actuators B* **133**, 97–104 (2008).
17. Pan, T. M. & Lin, J. C. Effects of post-deposition annealing and oxygen content on the structural and pH-sensitive properties of thin Nd_2O_3 films. *IEEE Sensors J.* **9**, 1173–1180 (2009).
18. Wu, M. H., Cheng, C. H., Lai, C. S. & Pan, T. M. Structural properties and sensing performance of high-k Sm_2O_3 membrane-based electrolyte-insulator-semiconductor for pH and urea detection. *Sen. Actuators B* **138**, 221–227 (2009).
19. Pan, T. M., Lin, J. C., Wu, M. H. & Lai, C. S. Study of high-k Er_2O_3 thin layers as ISFET sensitive insulator surface for pH detection. *Sen. Actuators B* **138**, 619–624 (2009).
20. Fu, X. Q., Wang, C., Yu, H. C., Wang, Y. G. & Wang, T. H. Fast humidity sensors based on CeO_2 nanowires. *Nanotechnology* **18**, 145503 (2007).
21. Izu, N., Itoh, T., Shin, W., Matsubara, I. & Murayama, N. C. O. sensor having two Zr-doped CeO_2 films with and without catalyst layer. *Electrochem. Solid-State Lett.* **10**, J37–J40 (2007).
22. Vaidya, S., Ahmad, T., Agarwal, S. & Ganguliw, A. K. Nanocrystalline oxalate/carbonate precursors of Ce and Zr and their decompositions to CeO_2 and ZrO_2 nanoparticles. *J. Am. Ceram. Soc.* **90**, 863–869 (2007).
23. Ansari, A. A., Solanki, P. R. & Malhotra, B. D. Sol–gel derived nanostructured cerium oxide film for glucose sensor. *Appl. Phys. Lett.* **92**, 263901 (2008).
24. Chiu, F. C. Thickness and temperature dependence of dielectric reliability characteristics in cerium dioxide thin film. *IEEE Trans. Electron Devices* **57**, 2719–2725 (2010).
25. Yang, S. M., Chien, C. H., Huang, J. J. & Lei, T. F. Nonvolatile flash memory devices using CeO_2 nanocrystal trapping layer for two-bit per cell applications. *Jpn. J. Appl. Phys.* **46**, 3291–3295 (2007).
26. Kao, C. H. *et al.* Effects of N_2 and O_2 annealing on the multianalyte biosensing characteristics of CeO_2-based electrolyte–insulator–semiconductor structures. *Sen. Actuators B* **194**, 503–510 (2014).
27. Zhao, Y., Kita, K., Kyuno, K. & Toriumi, A. Higher-k $LaYO_x$ films with strong moisture resistance. *Appl. Phys. Lett.* **89**, 252905 (2006).
28. Schroeder, T. *et al.* Titanium-added praseodymium silicate high-κ layers on Si(001). *Appl. Phys. Lett.* **87**, 022902 (2005).
29. Pan, T. M., Chang, K. Y., Lin, C. W., Tsai, S. W. & Wu, M. H. Label-free detection of uric acid using a disposable poly-*N*-isopropylacrylamide as an encapsulating enzyme material based on high-*k* $Eu_2Ti_2O_7$ electrolyte–insulator–semiconductor devices. *Sen. Actuators B* **160**, 850–857 (2011).
30. Wu, M. H., Lin, T. W., Huang, M. D., Wang, H. Y. & Pan, T. M. Label-free detection of serum uric acid using novel high-k Sm_2TiO_5 membrane-based electrolyte–insulator–semiconductor. *Sen. Actuators B* **146**, 342–348 (2010).
31. Pan, T. M., Wang, C. W., Weng, W. H. & Pang, S. T. Impact of titanium content and postdeposition annealing on the structural and sensing properties of $TbTi_xO_y$ sensing membranes. *J. Mater. Chem. C* **2**, 7575–7582 (2014).
32. Dang, V. S. *et al.* Electrical and optical properties of TiO_2 thin films prepared by plasma-enhanced atomic layer deposition. *Phys. Status Solidi A* **211**, 416–424 (2014).
33. Reddy, B. M. *et al.* Raman and X-ray photoelectron spectroscopy study of $CeO_2−ZrO_2$ and $V_2O_5/CeO_2−ZrO_2$ catalysts. *Langmuir* **19**, 3025–3030 (2003).
34. Ivanov, V. K., Shcherbakov, A. B. & Usatenko, A. V. Structure-sensitive properties and biomedical applications of nanodispersed cerium dioxide. *Russ. Chem. Rev.* **78**, 855–871 (2009).
35. Shannon, R. D. & Prewitt, C. T. Effective ionic radii in oxides and fluorides. *Acta Cryst. B* **25**, 946–954 (1969).
36. Teterin, Y. A. & Teterin, A. Y. Structure of X-ray photoelectron spectra of lanthanide compounds. *Russ. Chem. Rev.* **71**, 347–381 (2002).
37. Galtayries, A. *et al.* XPS analysis and microstructural characterization of a Ce/Tb mixed oxide supported on a lanthana-modified transition alumina. *Surf. Interface Anal.* **27**, 941–949 (1999).

38. Zhao, Y., Toyama, M., Kita, K., Kyuno, K. & Toriumi, A. Moisture-absorption-induced permittivity deterioration and surface roughness enhancement of lanthanum oxide films on silicon. *Appl. Phys. Lett.* **88**, 072904 (2006).

39. Nishikawa, Y., Yamaguchi, T., Yoshiki, M., Satake, H. & Fukushima, N. Interfacial properties of single-crystalline CeO_2 high-k gate dielectrics directly grown on Si (111). *Appl. Phys. Lett.* **81**, 4386–4388 (2002).

40. Bousse, L., De Rooij, N. F. & Bergveld, P. Operation of chemically sensitive field-effect sensors as a function of the insulator-electrolyte interface. *IEEE Trans. Electron Devices* **30**, 1263–1270 (1983).

41. Bergveld, P. & Sibbald, A. Comprehensive analytical chemistry: v.23: Analytical and biomedical applications of ion-selective field-effect transistors (Elsevier Science Publishing, 1988).

42. Shinwari, M. W., Deen, M. J. & Landheer, D. Study of the electrolyte-insulator-semiconductor field-effect transistor (EISFET) with applications in biosensor design. *Microelectron. Reliab.* **47**, 2025–2057 (2007).

43. Nicollian, E. H. & Brews, J. R. *MOS Physics and Technology* (Wiley, 1982).

44. Wang, Y. *et al.* Heterogeneous ceria catalyst with Water-Tolerant Lewis acidic sites for one-pot synthesis of 1,3-diols via prins condensation and hydrolysis reactions. *J. Am. Chem. Soc.* **135**, 1506–1515 (2013).

45. Burke, L. D. & Whelan, D. P. A voltammetric investigation of the charge storage reactions of hydrous iridium oxide layers. *J. Electroad. Chem.* **162**, 121–41 (1984).

46. Marzouk, S. A. M. *et al.* Electrodeposited iridium oxide pH electrode for measurement of extracellular myocardial acidosis during acute ischemia. *Anal. Chem.* **70**, 5054–5061 (1998).

47. Fog, A. & Buck, R. P. Electronic semiconducting oxides as pH sensors. *Sen. Actuators* **6**, 137–146 (1984).

48. Kim, T. Y. & Yang, S. Fabrication method and characterization of electrodeposited and heat-treated iridium oxide films for pH sensing. *Sen. Actuators B* **196**, 31–38 (2014).

49. Kao, C. H. *et al.* Multi-analyte biosensors on a CF_4 plasma treated Nb_2O_5-based membrane with an extended gate field effect transistor structure. *Sen. Actuators B* **194**, 419–426 (2014).

50. Liao, C. W., Chou, J. C., Sun, T. P., Hsiung, S. K. & Hsieh, J. H. Preliminary investigations on a glucose biosensor based on the potentiometric principle. *Sens. Actuators B* **123**, 720–726 (2007).

51. Jamasb, S., Collins, S. & Smith, R. L. A physical model for drift in pH ISFETs. *Sens. Actuators B* **49**, 146–155 (1998).

Acknowledgements

Author Contributions

TMP conceived experiments and data analysis and wrote manuscript. CWW and CYC assisted with experiment design and performed experiments and analyzed data. All authors discussed and commented on the manuscript.

Additional Information